JMEPEG
https://doi.org/10.1007/s11665-022-07426-8

©ASM International
1059-9495/$19.00

TECHNICAL ARTICLE

A Comparative Study on the High-Temperature Forming and Constitutive Modeling of Ti-6Al-4V

Murat Mert Uz, Afife Binnaz Hazar Yoruç, Cahit Sertaç Aydoğan, and Guney Guven Yapici

Submitted: 12 May 2022 / Revised: 8 August 2022 / Accepted: 20 August 2022

Ti-6Al-4V alloy is often preferred for high-performance components such as aerospace components due to its superior material properties and thermal resistance. In order to produce these components in the desired geometry, it is very important to determine the high-temperature thermomechanical properties of Ti-6Al-4V. In order to define these properties, uniaxial tensile tests at strain rates of 0.001, 0.01 and 0.1 s^{-1} at 700, 750 and 800 °C were applied in this study. In tests performed at a strain rate of 0.001 s^{-1} at 800 °C, an elongation at break above 0.8 representing a dominant ductile behavior is observed. It is clearly demonstrated that the initial 17.32% β phase reaches 31.02% at 800 °C, and the α grain size increases with temperature. Existence of dimples and voids in the fracture surfaces are an indicator of increased ductility behavior. In addition to the Modified Johnson–Cook model, which is widely used for modeling flow stress, the use of the extended Ludwik equation is suggested in this study. According to the correlation coefficient (R), it is claimed that the Extended Ludwik model is a more suitable approach for modeling the mechanical behavior for the studied forming temperature range.

Keywords constitutive modeling, hot forming, material characterization, Ti-6Al-4V alloy

1. Introduction

Ti-6Al-4V is the most widely used alloy of titanium in industrial applications and especially in aviation applications with its very good corrosion resistance and high strength. In the process of forming Ti-6Al-4V alloys at room temperature, there are disadvantages such as low-dimensional tolerance, tearing and high spring back problems (Ref 1, 2). Ti-6Al-4V alloys contain both α (hexagonal close-packed) and β (body-centered cubic) phases at room temperature. It is difficult to activate the deformation mechanism of prismatic, pyramidal and basal at room temperature (Ref 3). This situation reveals the necessity of forming Ti-6Al-4V at high temperatures, especially for parts with complex geometries. It has been observed that the studies generally concentrate on the forming of Ti-6Al-4V at superplastic temperatures. Therefore, this work is targeted to guide the hot forming processes taking place below the temperature range for superplasticity.

In recent years, researchers have evaluated the thermomechanical behavior of titanium at high temperatures from different perspectives. Vanderhasten et al. (Ref 4), in their study examining the mechanical properties, crystallographic and microstructural texture changes between room temperature and 1050 °C, determined the strain rate in the range of 0.05 to 0.0005 s^{-1}. It has been reported that strain hardening and dynamic recovery occur without dynamic recrystallization at temperatures below 600 °C, and dynamic grain growth occurs especially at 750 °C and at low strain rates. On the other hand, Markovsky et al. (Ref 5), in their study, examined the effects of strain rate on the mechanical strength at titanium and its alloys. They showed that the compressive mechanical behavior of titanium alloys is highly dependent on applied strain rate, phase composition and microstructure of the work material. In another study, the researchers investigated the plastic deformation properties of Ti-6Al-4V materials, with the application of tensile tests at very high strain rates (10^4 s^{-1}) from room temperature to 900 °C. They showed that machinability and hardening coefficient were related to strain rate as well as temperature, and ductility decreased with increasing strain rate (Ref 6).

Another issue of interest was the selected process temperature. Valoppi et al. (Ref 7) applied uniaxial tensile tests at high temperature and strain rates to investigate the plasticity, anisotropic properties, and microstructural evolution of sheet Ti-6Al-4V. As a result of the study, it was reported that the hardening coefficient and yield strength decreased with increasing temperature. In another study investigating the anisotropic behavior and mechanical properties of titanium alloys with α + β phase structure at high temperatures, uniaxial tensile tests were performed at 700 and 800 °C at quasi-static strain rates. It has been observed that the magnitude of anisotropy is weakened and the forming quality of Ti-6Al-4V alloy can be improved with increasing temperature or decreasing strain rate (Ref 8). Dineshkumar et al. (Ref 9) examined the tensile test results of 1.5 mm thick Ti-6Al-4V sheet material at constant strain rates at temperatures of 250, 450, and 650 °C. The results showed that maximum tensile strength and yield

Murat Mert Uz and **Afife Binnaz Hazar Yoruç**, Department of Metallurgical and Materials Engineering, Faculty of Chemical and Metallurgical Engineering, Yildiz Technical University, Esenler, Istanbul, Turkey; **Cahit Sertaç Aydoğan**, Turkish Aerospace Industries, Fethiye Mahallesi, Kahramankazan, Ankara, Turkey; and **Guney Guven Yapici**, Mechanical Engineering Department, Ozyegin University, Istanbul, Turkey. Contact e-mails: mmertuz@gmail.com and mert.uz@std.yildiz.edu.tr.

Published online: 28 September 2022

strength decrease and percentage elongation increases with increasing temperature. At temperatures above 650 °C, the maximum tensile strength is approximately 66% lower than the maximum tensile strength at room temperature. In another exemplary study on the mechanical characterization of titanium alloys at high temperatures, a compression test was applied to Ti-6Al-4V materials to which different boron ratios were added, from room temperature to 700 °C, at strain rates of 0.001, 0.1, and 1 s^{-1} (Ref 10).

Constitutive equations were developed to describe the flow behavior of materials as a function of strain rate and temperature, and are used for modeling complex structures exposed to different conditions. Constitutive equations can be categorized as phenomenological, physically based, and structural neural network models. All these models require mechanical experiments to determine the model parameters (Ref 11-14). Cingara, the hyperbolic sine equation, and Shafiei-Ebrahimi equations were used in the study, which aims to model the yield behavior of Ti-6Al-4V in the range of 900-1050 °C. Approaches using modified Cingara and Shafiei-Ebrahimi equations have reached the highest accuracy (Ref 15). In a study comparing the Johnson–Cook equation and the modified Johnson–Cook equation, which are frequently used material models in sheet metal forming, it was revealed that the modified Johnson Cook model is much more suitable (Ref 16). However, unlike the Johnson–Cook model for high temperatures, there are some studies on the extended Ludwik equation. In order to model the thermomechanical properties of AA3104 and AA5182 alloys up to 500 °C, Haaften et al. proposed the extended Ludwik equation (Ref 17). Similarly, Soni et al. (Ref 18) used the extended Ludwik equation to predict the high-temperature flow behavior of cast aluminum alloys. In addition to the modified Johnson–Cook model for modeling the mechanical properties of Ti-6Al-4V at high temperatures, the extended Ludwik equation, which is used in the literature for aluminum alloys and magnesium alloys, was preferred in our study (Ref 19, 20). The reason for choosing these two empirical models is that they can be easily integrated into commercial finite element software and the determination of their coefficients is simpler than physical models.

In this study, the high-temperature mechanical properties, fracture behavior, transformation of microstructure, and phase distribution of Ti-6Al-4V, which is needed for hot forming of Ti-6Al-4V alloy, and formation of the constitutive equation are focused. For this reason, hot tensile tests were applied at temperatures of 700, 750 and 800 °C and at quasi-static strain rates. High-temperature flow behavior and the resulting microstructural variations were determined from these tests. Extended Ludwik equation, which was not preferred for Ti-6Al-4V material before, was used for structural modeling, and its accuracy was compared with the modified Johnson–Cook model. In addition, the relationship between fracture behavior and the temperature was evaluated for samples subjected to tensile strain at a wider temperature range.

2. Material and Method

2.1 High-Temperature Tensile Tests

For the high-temperature tensile tests, 2 mm thick Ti-6Al-4V sheet material supplied by Turkish Aerospace Industries Inc. (TUSAŞ) was used. The chemical composition of the material is given in Table 1. The chemical composition of the samples complies with ASTM B348/B348M standard (Ref 21).

The cutting process of the samples used in the experiments was carried out with a high precision water jet and the plate was cut parallel to the rolling direction. Samples were sized following the ASTM E8/E8M-11 standard and sample sizes are shown in Fig. 1 (Ref 22). It is known that material texture plays an important role in the mechanical response of Ti6Al4V, though only samples cut parallel to the rolling direction were used in the study. This is mainly because the anisotropic mechanical characteristics of the alloy weakens with increasing temperature or decreasing strain rate, where the effect of texture is typically neglected at high temperatures (Ref 8, 23–27). Therefore, this study concentrates solely on the predictive capability of various constitutive models in the high-temperature forming regime. Nevertheless, detailed emphasis on anisotropy is planned to be a topic of a future work.

Uniaxial tensile tests were carried out at temperatures of 700, 750 and 800 °C with strain rates of 0.001, 0.01 and 0.1 s^{-1}. Additional tests were carried out at temperatures of 500 and 600 °C and at a strain rate of 0.1 s^{-1}. All tests are performed and sample codes are shown in Table 2. For high-temperature uniaxial tensile tests, an Instron mechanical test frame was used. Heating of the test pieces in the system was provided by the induction system, and temperature monitoring was provided by an infrared thermal camera. As the experiments were conducted with an induction heating system, it was possible to prevent oxidation and related mechanisms such as alpha case formation and eliminate its effect on the flow behavior.

The specimens were quenched at the end of the test to retain their fracture surface and existing microstructure. Thus, it was possible to examine the microstructural changes at high temperatures. For each parameter set, the tests were performed in triplicate to obtain reproducible results.

2.2 Microstructural and Fracture Surface Examinations

Microstructural examination of the region from the fracture surfaces of the materials to the end of the gauge length was carried out. The samples were first hot-mounted and then mechanically sanded with SiC sandpaper up to 2400 grit. Polishing was done with 6 and 1 μm diamond solutions. Kroll's reagent (2% HF + 3% HNO_3 + 95% H_2O) was used for etching. The microstructure of the samples was examined with optical microscope (OM) images at different magnifications. ImageJ digital image processing software was used to determine the area fraction of the phases and average grain size from the images. A schematic representation of the observed region and fracture surfaces where the microstructural examinations were made is given in Fig. 2.

To examine the fracture surfaces of Ti-6Al-4V specimens which were subjected to hot tensile tests at different temper-

Table 1 Chemical composition of Ti-6Al-4 V sheet material

Element	Al	V	Fe	Ti
%weight	5.78	3.84	1.27	Balanced

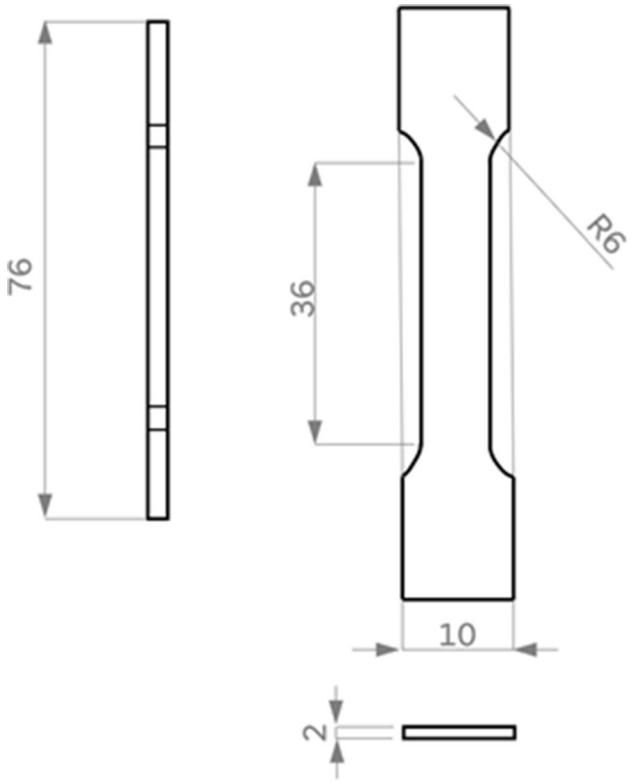


Fig. 1 Tensile test specimen geometry (all dimensions in mm)

Table 2 Information of all high-temperature tensile test groups

Sample	Temperature, °C	Strain Rate, s^{-1}
500C-0.1	500	0.1
600C-0.1	600	0.1
700C-0.1	700	0.1
700C-0.01	700	0.01
700C-0.001	700	0.001
750C-0.1	750	0.1
750C-0.01	750	0.01
750C-0.001	750	0.001
800C-0.1	800	0.1
800C-0.01	800	0.01
800C-0.001	800	0.001

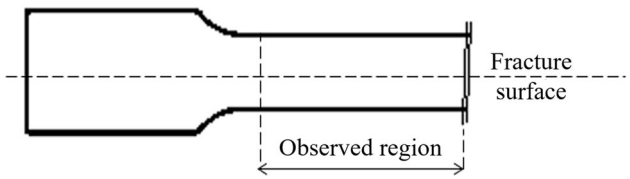


Fig. 2 Schematic representation of the examined regions of the samples

atures and strain rates, the fracture regions were examined at different magnifications by a scanning electron microscope (Thermo Scientific™ Quattro S).

3. Results and Discussion

3.1 Microstructural Examination

In an effort to examine the microstructural effects of temperature and deformation rate on the hot tensile test specimens, the images of the specimens subjected to the test at different magnifications were examined by optical microscope. The microstructure of the initial material is shown in Fig. 3. α and β phase ratios and grain sizes were examined where light colored areas show α grains and dark areas show β grains. According to the microstructure image, the β phase ratio was calculated as 17.3% and the α phase ratio as 82.7%. As it can be seen in Fig. 3c and Fig. 3d, the average size of α grains was 5.34 μm. The room temperature microstructure consists of equiaxed α phase grains with a homogeneous distribution of the fine intergranular β phase. The microstructure images obtained are similar to the studies of Mosleh et al. on high-temperature forming of bi-phase titanium alloy in the temperature range of 750-900 °C (Ref 28).

In Fig. 4, optical microscope images of the fracture surfaces of the tests at a strain rate of 0.1 s^{-1} at and 500, 600, 700, 750 and 800 °C are given to examine the effect of temperature on the microstructure. β phase ratios were calculated from the images. In Fig. 4f, the image of the sample processed in the ImageJ software at 800 °C is given as an example. The same procedure was applied to other samples.

When the microstructures of the samples tested at high temperatures were compared with the initial sample, it was observed that the ratio of the β phase increased and the homogeneity of the β phase decreased partially. However, in almost all deformation conditions, the microstructures exhibited equiaxed grains resembling the initial microstructural morphology. In Fig. 5, graphs showing the variation of the ratio of the β phase and the average size of the α grains with temperature are given.

From Fig. 5a, while the β phase has an area of approximately 17.32% at room temperature, it is clearly seen that this ratio increases with increasing temperature. This ratio was calculated to be 19.12% at 500 °C, 19.49 at 600 °C, and 25.95% β phase ratio was calculated when the temperature increased to 700 °C. No significant change was observed between 700 °C and 750 °C. At 800 °C, the β phase ratio reached the highest value as 31.02%. The data obtained is parallel with the β transus temperature being 980 °C (Ref 29). Jiao et al. (Ref 30) investigated the phase structures above 800 °C in their study and reported that in the α + β two-phase region, the grain size curves changed with the rise of test temperature and the volume fraction of the primary α phase reduced with the remain of the deformation temperature. The graph of the variation of the mean grain size of the α phase with temperature is given in Fig. 5b. The trend of change in the mean size of α grains with temperature was similar to the variation in the β phase. It was determined that the average grain size of α, which was measured as 5.34 μm in the initial microstructure, enlarged with rising temperature. The average grain size of 6.46 μm at 500 °C and 6.93 μm at 600 °C was measured. At 700 °C, the α grains in the microstructure were found to be 8.64 μm on average, 8.84 μm at 750 °C and 9.01 μm at 800 °C. These results are similar to the results of the study reported by Zhang et al. (Ref 31).

To investigate the effect of the strain rate on the microstructure at the same temperature, the samples that were subjected to

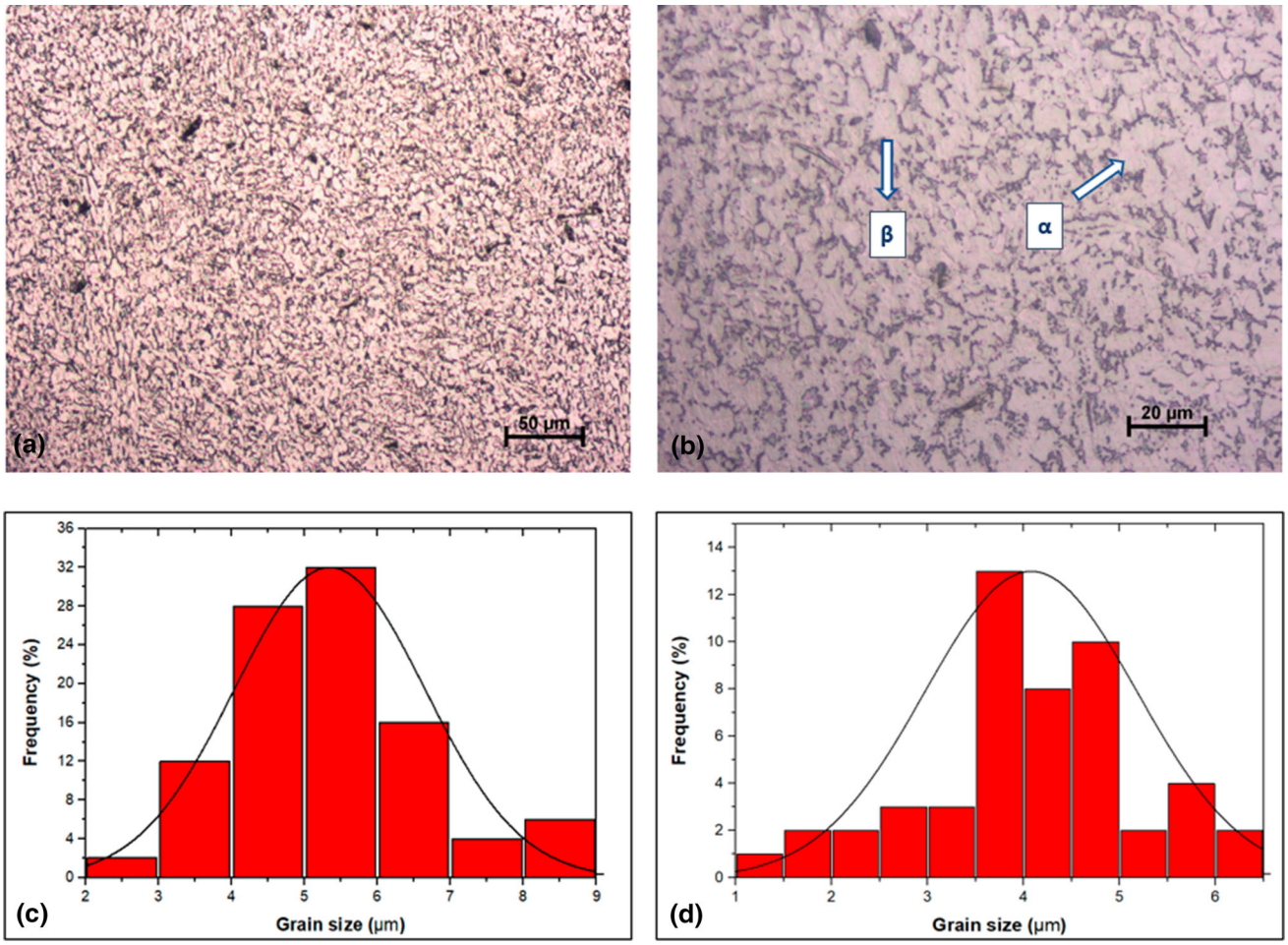


Fig. 3 Optical microscope images of the as is sample at, (a) 200, (b) 500 magnifications; (c) α grain size distribution, (d) β grain size distribution

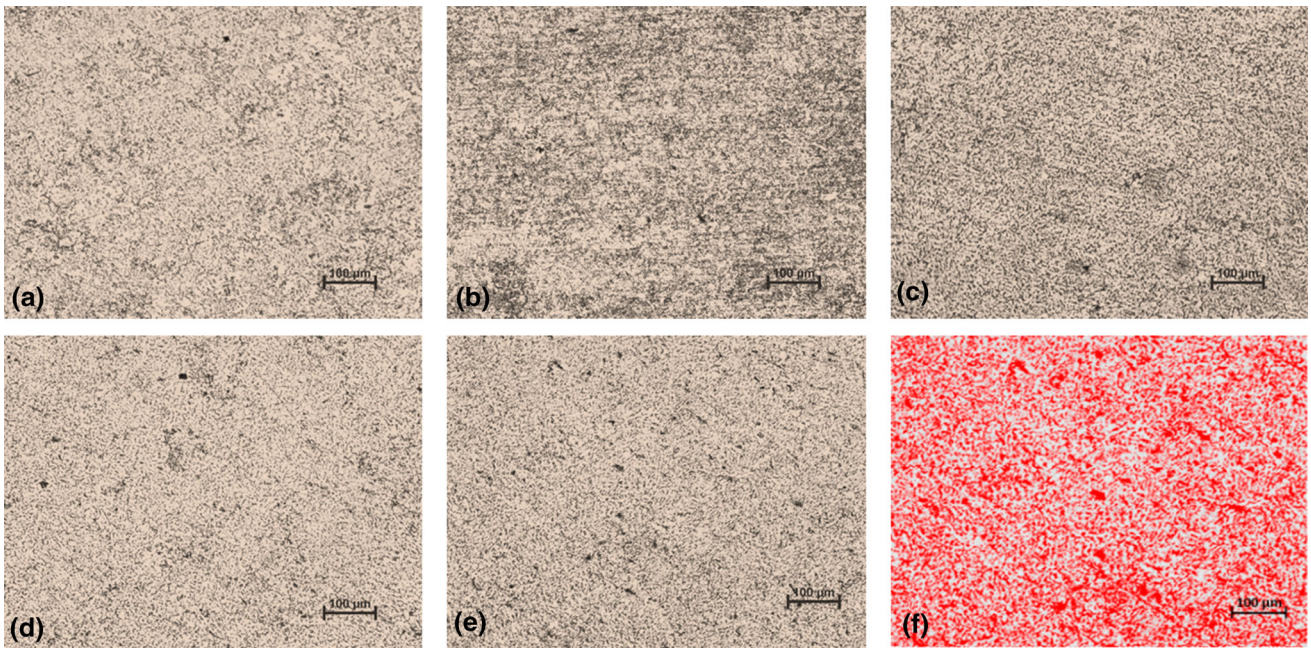


Fig. 4 Optical microscope images at X100 magnification of fractured specimens at a strain rate of 0.1 s^{-1} and at different temperatures of (a) 500 °C, (b) 600 °C, (c) 700 °C, (d) 750 °C, (e) 800 °C, (f) processed image of 800C-0.1 sample

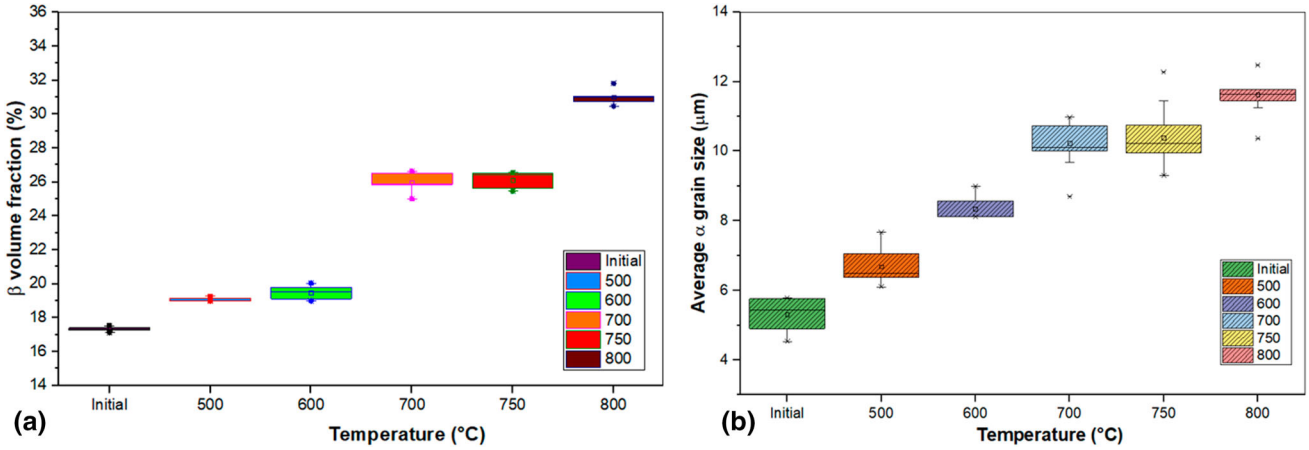


Fig. 5 At strain rate of 0.1 $s.^{-1}$, at different temperatures (a) volume fraction of β phase (%), (b) average α grains size (μm)

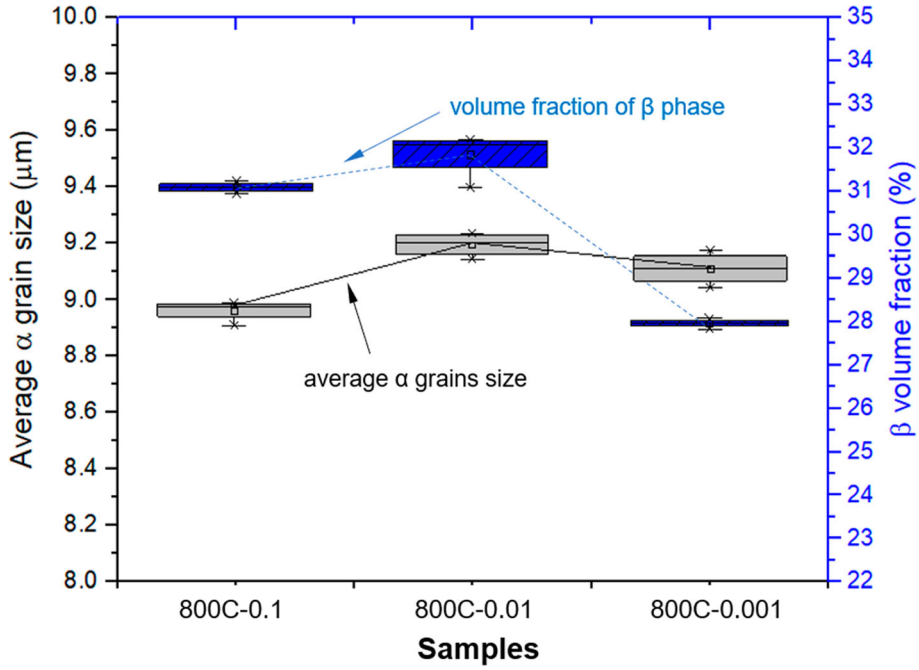


Fig. 6 Volume fraction (%) of β phase and mean size of α grains (μm) for tests at 800 °C at different strain rates

tensile strain at a strain rate of 0.001, 0.01 and 0.1 s^{-1} at 800 °C were examined. In Fig. 6, the average grain size of α and the β phase ratio, calculated as a result of the examinations at the fracture zones of the samples at different strain rates at 800 °C, are given. It has been observed that there is no significant change in the volumetric ratio of the β phase and the average size of the α grains at these strain rates. There could be two main reasons for this. First, the sample, which heats up very quickly in the induction heating system, may not have found the necessary time for microstructural transformation because it was cooled quickly after the test. The second factor is that since all applied deformation rates are in the quasi-static scale, it is normal not to observe a noticeable change.

3.2 High-Temperature Tensile Behavior

The true stress–strain curves of the material under the specified test conditions are given in Fig. 7. It is quite evident in Fig. 7 that the yield strength values at high strain rates and low temperatures are much greater than the yield strength values at high temperatures. Similarly, it has been revealed that the strains are higher, especially at high temperatures and low deformation rates. When the curves at the same temperature values and different strain rates are examined, it can be seen that the material behaves similarly at each distinct temperature. Results were consistent with the studies conducted by Gao et al., in which they investigated the hot drawing deformation behavior of Ti-6Al-4V sheet material in the temperature range of 650-750 °C and strain rate range of 0.001-0.1 s^{-1} (Ref 32).

The yield strength, maximum tensile stress and elongation at break values of each sample were obtained from true stress–strain curves. Figure 8 shows the change in these properties with respect to temperature and deformation rate. It can be observed from Fig. 8a that the yield strength and the maximum tensile strength decrease as the temperature increases; this can be due to diffusion, heat softening and dislocation mobility

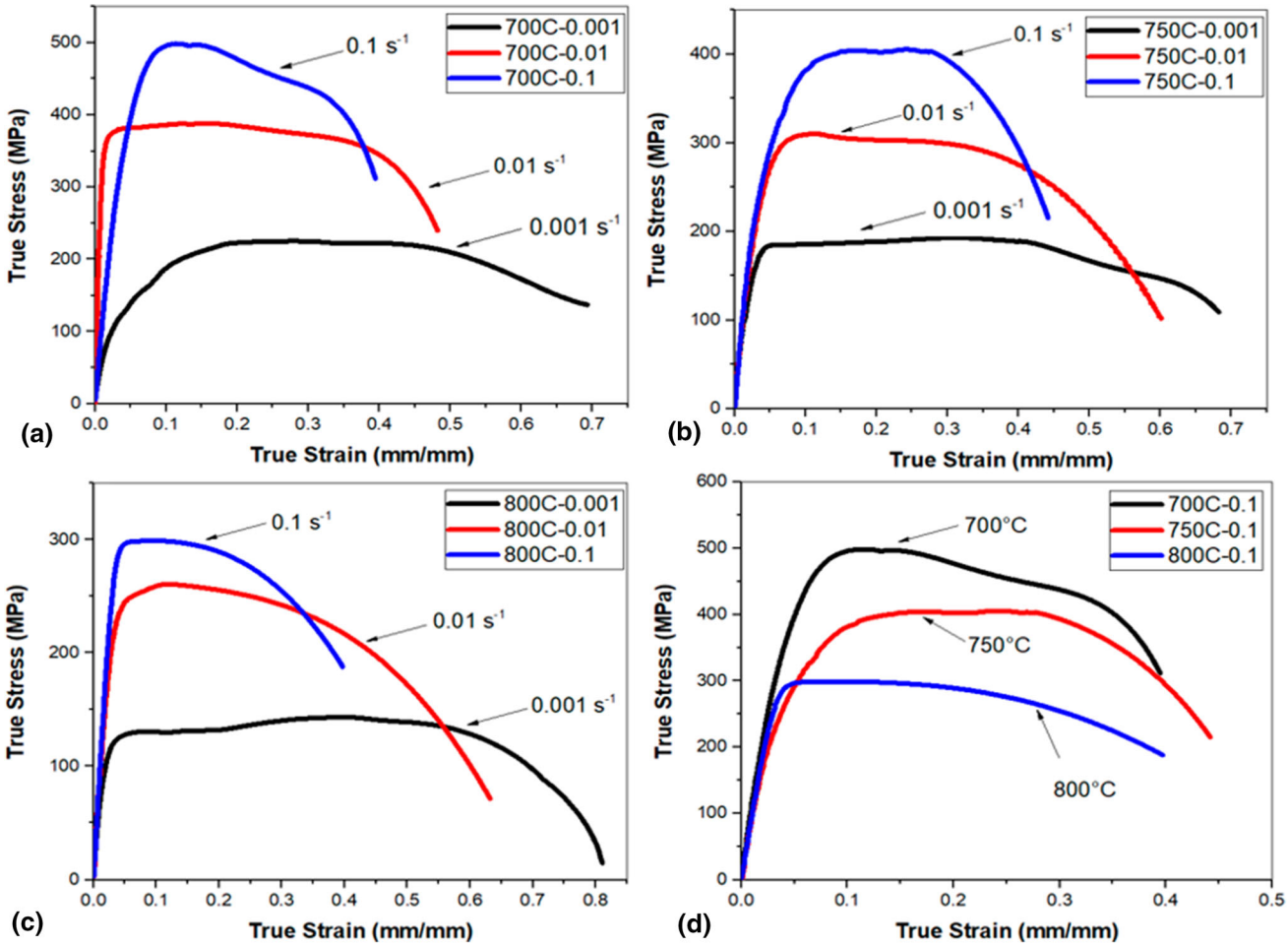


Fig. 7 Stress–strain curves in Ti-6Al-4 V alloy at (a) 700 °C, (b) 750 °C, (c) 800 °C at different strain rates, (d) 0.1 s^{-1} strain rate at different temperatures

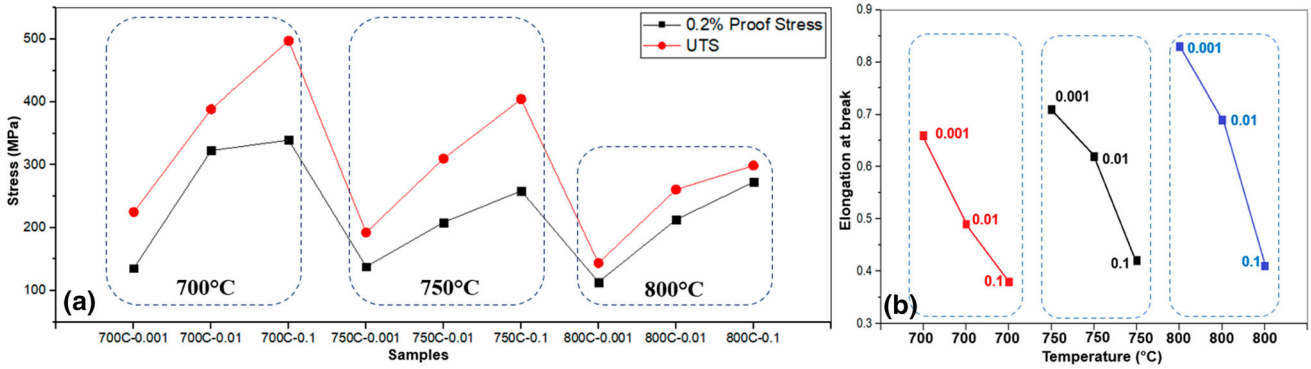


Fig. 8 At different temperatures and strain rates; (a) 0.2% proof stress and ultimate tensile strength, (b) elongation at break values

(Ref 33). As the temperature increases, the thermal activation mechanism in the material becomes more effective. The absorbed kinetic energy of each atom increases, resulting in an increase in the amplitude of the atomic vibration. In addition, the Gibbs free energy required for dislocations to cross the energy barrier decreases. Thus, the mobility of dislocations, slip systems and gaps increases. This increases the metal plasticity and reduces the material strength (Ref 34).

At the same time, the increase in temperature accelerates the dynamic recrystallization (DRX) and dynamic recovery (DRV) of the deformed Ti-6Al-4V grains. This situation creates a softening effect in the material. The combined effect of these factors causes the shear stress to decrease. This causes a reduction in the flow stress of the Ti-6Al-4V alloy (Ref 34, 35). At the same temperature the sensitivity of the material to strain rate is examined, that decreasing strain rate also reduces the yield stress, as stated before. The main reason for this is dislocation movements, and the material reaches higher strengths since the necessary time for the accumulation of dislocations cannot occur at high deformation rates (Ref 36). In

addition to this idea, it has been reported that low deformation rate ensures more time for DRV and DRX mechanisms during deformation, increasing ductility (Ref 37). The elongation at break values reported in Fig. 8b is also increased with increasing temperature and decreasing strain rate. In particular, in the test performed at a strain rate of 0.001 s^{-1} at 800 °C, the specimen exhibited the highest elongation until fracture. In a study carried out with a similar forming temperature range, it was observed that the 800 °C-0.001 s^{-1} condition approached the superplasticity limit (Ref 38). It has been reported that the elongation at break values are directly related to the initial microstructure. The information obtained from the results showed that the elongation at break values of the equiaxed microstructure is in accordance with the literature (Ref 39).

Accordingly at high temperature ductility increases due to grain boundary sliding and β-phase transformation. The fact that the yield stress decreases with the increase in the β phase ratio in similar regimes confirms this idea. In addition to dynamic recrystallization at a deformation rate of 0.001 s^{-1} at 800 °C, the grain boundary sliding mechanism also comes into play. In the comparison made for grain boundaries, it is known that the shear strength of α/α boundaries is higher than that of α/β grain boundaries. Therefore, increasing α/β grain boundary with increasing β phase will increase ductility (Ref 31). The relationship between the β phase in the structure and the formability can be explained with this reasoning. Much higher temperatures (above 900 °C) will cause the dominant phase to become β, in which case much higher strain values will be reached when very low strain rates are used.

3.3 Fracture Surface Characterization

Figure 9 shows the SEM images to determine the behavior of fracture surfaces of specimens subjected to tensile testing at different temperatures at a constant strain rate (0.1 s^{-1}). Fracture surface areas were calculated from these images taken at low magnifications, and the ductile–brittle transition behavior was characterized. Figure 9a shows a selected surface sample for calculating the fracture surface area.

In Fig. 9a-e, the ruptured surfaces at different temperatures are examined. It has been determined that the rupture is more fragmented in large areas at lower temperatures, and the fracture surface area in the material decreases with the increase in temperature. Due to little or no neck formation during brittle fracture, the fracture surface area is expected to be larger than in the ductile fracture behavior where neck formation can be achieved. These results confirm that the material exhibits ductile behavior with increasing temperature, and they are in line with the elongation at break data given in Fig. 8b (Ref 40). As seen in the graph of the fracture surface areas and the temperature relationship given in Fig. 9f, especially at the 500 °C-600°C transition, a dramatic decrease in the fracture surface area was observed. The fracture surface area, which was over 4.0 mm^2 at 500 °C, decreased to 2.05 mm^2 at 600 °C. Above 600 °C, although the ductile behavior continues and increases, there is no marginal decrease in fracture surface area. The fracture surface area was calculated as 1.71 mm^2 at a strain rate of 0.1 s^{-1} at 700 °C and 1.14 mm^2 at 800 °C.

In search of the effect of strain rate on fracture behavior, the fracture surfaces of the samples tested at the same temperature and different strain rates were investigated. As an example, SEM images of fracture surfaces at 800 °C at three different strain rates and a graph of fracture surface areas are given in Fig. 10a-c. In Fig. 10d, a graph showing the relationship of fracture surface areas with both temperature and strain rate is given. As it can be seen, the fracture surface areas of samples at strain rate of 0.001 s^{-1} are much smaller compared to samples at higher strain rates. The fracture surface of 800C-0.001 sample was measured as 0.325 mm^2. The fracture surface area obtained from the 800C-0.001 sample, which includes the combined effect of high temperature and low strain rate, is the sample showing the most ductile behavior in this study. The fracture surface area was measured as 0.83 mm^2 when the strain ratio was 0.01 s^{-1}, and 1.14 mm^2 when it was 0.1 s^{-1}. In other words, it has been seen that decreasing deformation rate, like increasing temperature, leads the material to ductile behavior. The effect of strain rate on the fracture surface area had a

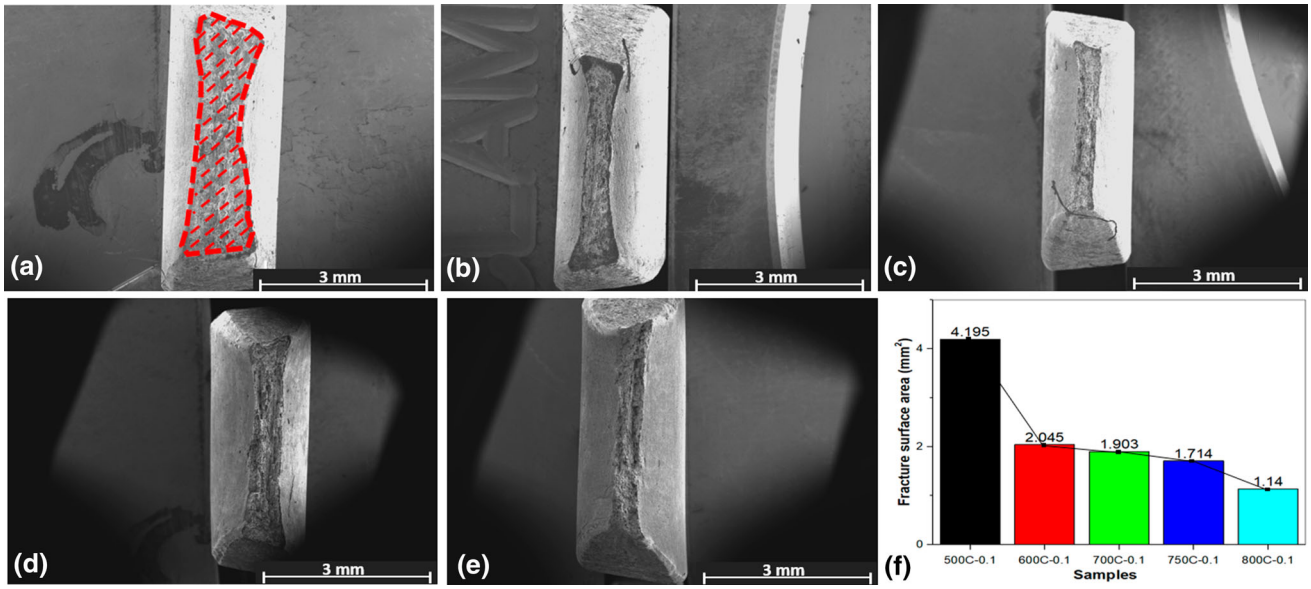


Fig. 9 SEM images of fracture surfaces at strain rates of 0.001 s^{-1} at X60 magnification (a) 500 °C, (b) 600 °C, c) 700 °C, (d) 750 °C, (e) 800 °C and (f) relation of fracture surface areas with temperature

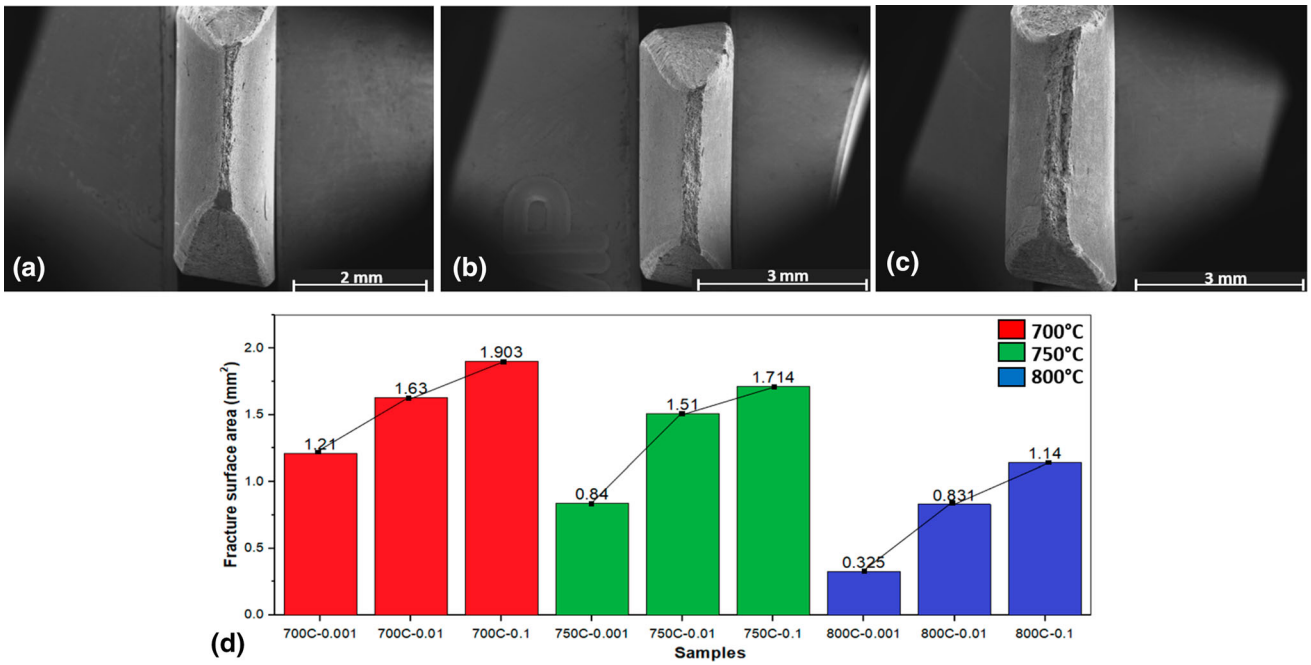


Fig. 10 SEM images of fracture surfaces at X60 magnification at 800 °C (a) 0.001 s^{-1}, (b) 0.01 s^{-1}, (c) 0.1 s^{-1} and (d) relationship of fracture surface areas with strain rate

similar effect at all temperature values. In the study examining fracture behavior and the mechanical properties of commercial pure titanium and Ti-6Al-4V, the relationship of microstructure and deformation parameters with the fracture surface was revealed (Ref 41). Wahed et al., in their study examining the superplastic properties of Ti-6Al-4V sheet materials, observed that the number of voids increases and the size decreases as the strain rate increases for a constant temperature in fracture surfaces that occur slightly below the superplastic temperature (Ref 33). These findings are compatible with both the determined mechanical properties and the information stated in the literature that high temperature and low deformation rate increase the formability (Ref 42-44).

In another examination made from the fracture surfaces of the samples, the characteristics of flow lines, voids and dimples were observed. Samples were examined from both the middle and upper parts of the fracture surfaces. In Fig. 11, the examination of the 800C-0.1 sample is given as an example. Similar procedure was applied to other samples.

In order to examine the effects of the strain rate while keeping the temperature constant, SEM images at different magnifications are given in Fig. 12 from the middle part of the sample at 700 °C and 800 °C. For a constant temperature, it can be observed that the number of voids increases and the size decreases as the strain rate increases. The void size was measured as approximately 8.22 μm at a strain rate of 0.001 s^{-1} at 800 °C deformation temperature, 7.59 μm at a strain rate of 0.01 s^{-1} and 6.96 μm at a strain rate of 0.1 s^{-1}. The void density was found to be higher at low strain rates. Similarly, in the examination of the hot tensile test fracture surfaces test specimens at 700 °C, the void size was measured as approximately 5.31 μm at a strain rate of 0.001 s^{-1}. It was observed that the gap size was 4.71 μm at 0.01 s^{-1} strain rate and 4.63 μm at 0.1 s^{-1} strain rate. These values prove that as the deformation rate increases, the size of the void decreases and the number increases. By comparing both data, it is possible to comment on the fracture behavior at different temperatures at the same strain rate. From this, it has been determined that increasing temperature increases the size and amount of voids (Ref 45).

In order to look at the impact of temperature, SEM images of fracture surfaces from 500 to 800 °C and strain rate of 0.1 s^{-1} are given in Fig. 13. As it can be seen from Fig. 13, the increase in ductility can be expressed in terms of the increase in the amount of voids and flow lines, and the main factor causing the increase in ductility is temperature. It is seen that increasing temperature increases the amount of voids and ductile fracture flow lines in fracture areas. Another conclusion that can be drawn from these results is that the dimple size is partially small under low temperature conditions; at high temperatures, it is much larger than the dimple size. Figure 13d shows that ductile deformation behavior dominates, which we can infer from the presence of large sized dimples, voids and flowlines. On the contrary, as in Fig. 13a, it was observed that fracture occurred before creating sharper fracture zones, void and dimple formation at low temperatures. In these images, the dispersed particles are considered to be impurities.

3.4 Modeling of Mechanical Behavior

3.4.1 Extended Ludwik Model. Typically, the flow behavior data of materials are used to construct primary models for predicting the flow stress state at varying deformation rates and different temperatures. The Ludwik model is one of the empirical models developed for the mathematical expression of the experimentally obtained real stress-true elongation curves (Ref 46).

$$\sigma = K\varepsilon_{pl}^{n} \quad \text{(Eq 1)}$$

Since the Ludwik equation does not specifically describe the flow behavior with varying temperature, Haaften et al. have proposed the Extended Ludwik equation (Ref 17).

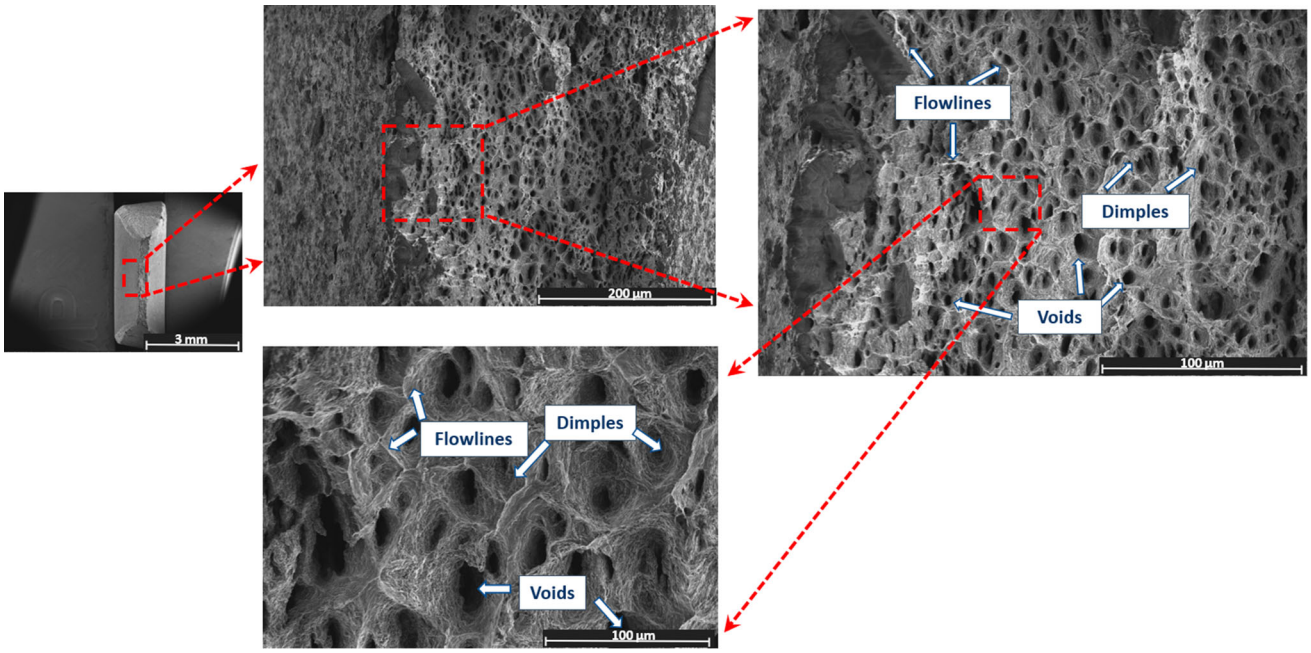


Fig. 11 SEM images of the fracture surface of the test performed at 800 °C at a strain rate of 0.1 $s.^{-1}$

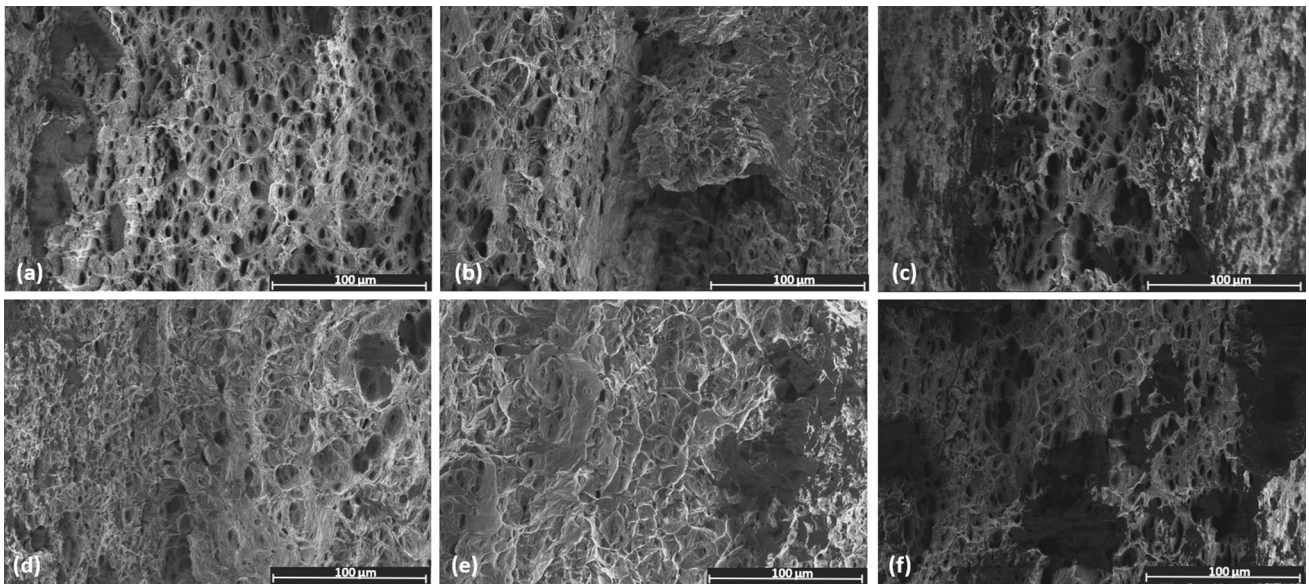


Fig. 12 SEM images of fracture surfaces at 800 °C (a) 0.1, (b) 0.01 and (c) 0.001 s^{-1} strain rate, 700 °C (d) 0.1, (e) 0.01 and (f) 0.001 s^{-1} strain rate

$$\sigma = K\left(\dot{\varepsilon} + \dot{\varepsilon}_{p^0}\right)^m \left(\varepsilon_p + \varepsilon_{p^0}\right)^n \quad \text{(Eq 2)}$$

In Eq. 2, σ represents true stress (MPa), ε_p the true strain and $\dot{\varepsilon}_p$ the strain rate (s^{-1}). In addition, K is the strength coefficient, n is the hardening coefficient, and m is the strain rate sensitivity coefficient. $\dot{\varepsilon}_{p^0} = 10^{-4}$, $\varepsilon_{p^0} = 10^{-6}$ are numerical constants specified (Ref 46). In order to find n, the data obtained at strain rates in the range of 700-800 °C under strain rate conditions are used. The partial derivatives of the natural logarithms of strain and stress were calculated from these data $\left(n = \frac{\partial ln\sigma}{\partial ln\varepsilon}\right)$.

In order to shorten the calculation time, 0.10, 0.15, 0.20, 0.25, 0.30 and 0.35 were chosen as strain points. Figure 14a shows the experimental lnσ plot corresponding to lnε at 700 °C. At each strain rate, the slope was found by linear regression for data for which the slope represents the n-parameter. To evaluate the n-parameter, an average of the slope values obtained at different strain rates between 700 and 800 °C was taken.

In order to determine the value of m, it is necessary to determine the sensitivity of stresses at different real strain values according to the strain rate. Consequently, take the

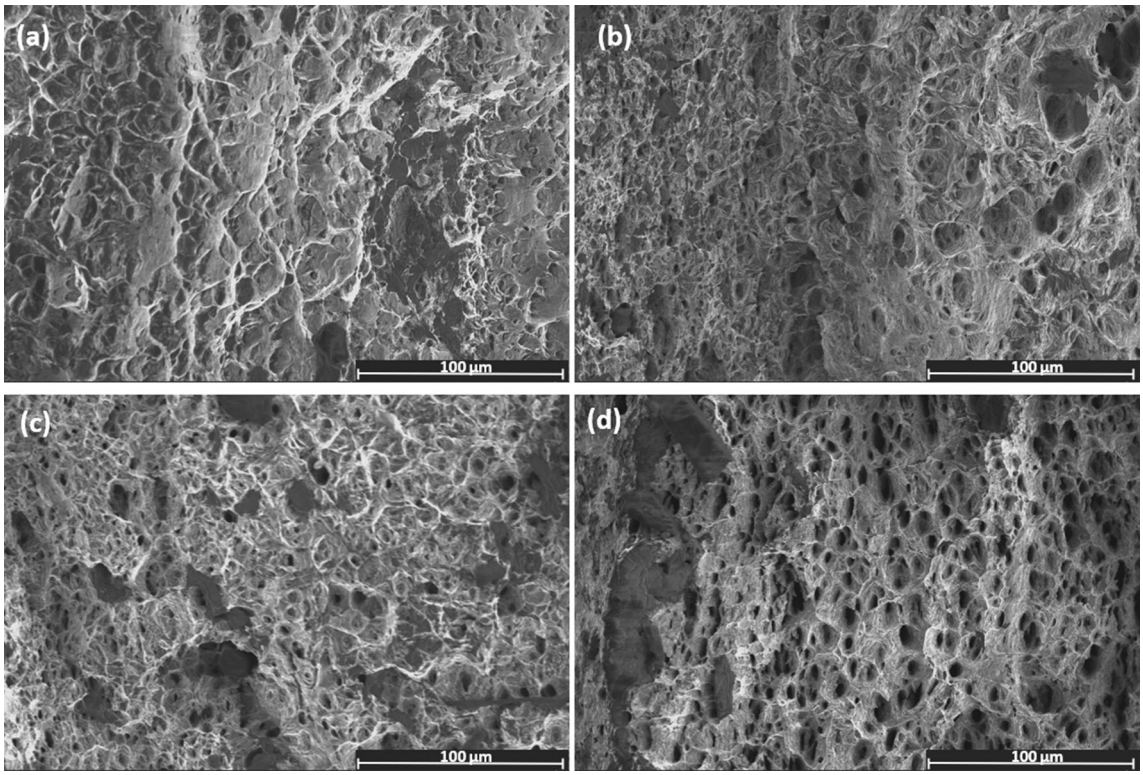


Fig. 13 SEM images of fracture surfaces at a strain rate of 0.1 s^{-1} (a) 500 °C, (b) 600 °C, (c) 700 °C and (d) 800 °C

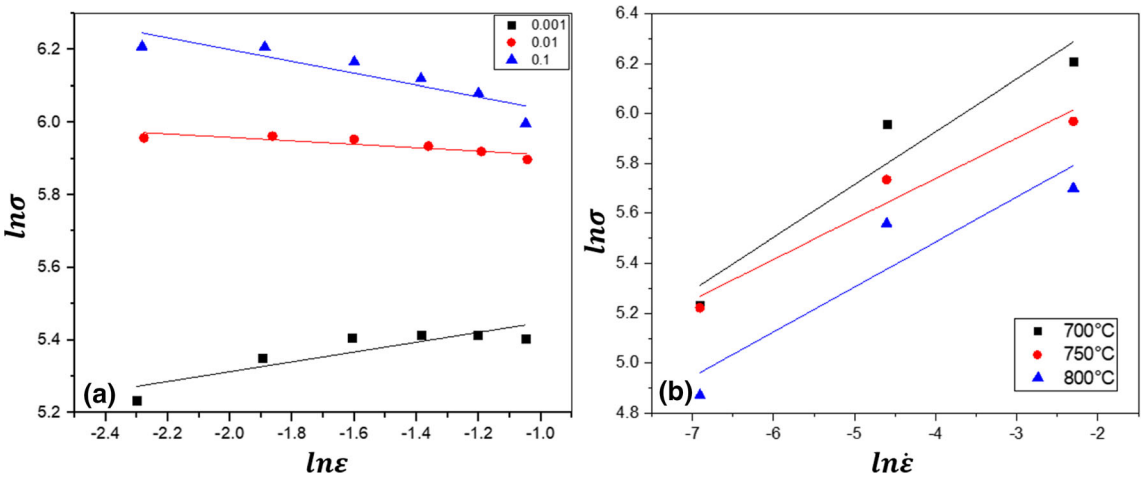


Fig. 14 lnε-lnσ plot at 700 °C, (b) lnέ – lnσ plot at different strain rates at 0.1 strain value

derivatives of the natural logarithms of the strain rate and stress. ($m = \frac{\partial ln\sigma}{\partial ln\dot{\varepsilon}}$). Figure 14b shows the graph of lnέ – lnσ at different strain rates at 700, 750 and 800 °C. The slopes of the data give m for each temperature value.

The K value is adapted to empirical results in the Extended Ludwik equation, using an iterative process to arrive at a reliable result. In order to understand the effect of strain rate on flow stress, Eq. 2 is arranged and Eq. 3 is formed, C coefficient is obtained. The K value for each temperature can be found by establishing a ratio between the coefficient C and K.

$$\sigma = K\left(\dot{\varepsilon} + \dot{\varepsilon}_{p^0}\right)^m \left(\varepsilon_p + \varepsilon_{p^0}\right)^n = KC \qquad \text{(Eq 3)}$$

Table 3 Coefficients for the e-Ludwik material model

Temperature, °C	K	M	n	$\dot{\varepsilon}_{p^0}$	ε_{p^0}
700	860.19	0.2116	− 0.0024	1E-06	1E-04
750	576.52	0.1621	− 0.0190	1E-06	1E-04
800	431.51	0.1802	− 0.0747	1E-06	1E-04

The material constants determined for the e-Ludwik model are presented in Table 3.

3.4.2 Modified Johnson–Cook Model. Johnson–Cook material model is a phenomenological model that describes stress by considering the effects of strain, strain rate and temperature. This model is suitable for describing the stress and strain relationships of metallic materials under conditions of large deformation, high strain rate, and high temperature, and Johnson and Cook proposed in 1985 (Eq. 4) (Ref 48):

$$\sigma = (A + B\varepsilon^n)\left(1 + C\ln\left(\frac{\dot{\varepsilon}}{\dot{\varepsilon}_0}\right)\right)\left[1 - \left(\frac{T - T_r}{T_m - T_r}\right)^m\right] \quad \text{(Eq 4)}$$

A parameter in Eq. 4 represents yield strength (MPa), B hardening parameter (MPa), n hardening coefficient, C stress ratio sensitivity coefficient, $\dot{\varepsilon}^*$ dimensionless plastic strain rate, T* dimensionless temperature value, m thermal softening coefficient.. The dimensionless plastic strain ratio $\dot{\varepsilon}^*$ is expressed as the ratio of plastic strain ($\dot{\varepsilon}$) to the reference strain. The reference temperature T in the T* equation represents the room temperature T_r and the melting temperature T_m.

In the first JC model presented, thermal softening, strain rate hardening, and strain hardening are considered as three independent phenomena (Ref 47). To improve accuracy, Lin et al. modified the Johnson–Cook model and proposed the Modified Johnson–Cook (m-JC) model (Eq. 5) (Ref 49).

$$\sigma = \left(A_1 + B_1\varepsilon + B_2\varepsilon^2\right)(1 + C_1 ln\dot{\varepsilon}^*)\exp[(\lambda_1 + \lambda_2 ln\dot{\varepsilon}^*)(T - T_r)] \quad \text{(Eq 5)}$$

It is estimated that the stress values obtained with the one-dimensional quadratic or cubic equation in the m-JC model will have a high accuracy rate compared to the standard JC model. For this reason, the first bracket denoting the strain sensitivity was determined by the second- and third-order formulations. Other statements have been revised accordingly. A_1, B_1, B_2, B_3, C_1, λ_1 and λ_2 in Eq. 5 are all material-related parameters and the other expressions have the same meaning as in the JC model (Ref 13).

A_1, B_1, B_2, B_3 values can be evaluated by constructing a polynomial suitable for the relationship between stress and strain. The coefficients of the quadratic polynomial of the σ-ε graph in Fig. 15a have been determined, these coefficients give the coefficients A_1 = 145.09 B_1 = 2260 and B_2 = -6982.9.

In order to determine the C_1 parameter, Eq. 5 can be arranged as Eq. 6, under conditions where the deformation temperature is the reference temperature. Then, Eq. 7 is obtained.

$$\sigma = \left(A_1 + B_1\varepsilon + B_2\varepsilon^2\right)(1 + C_1 ln\dot{\varepsilon}^*) \quad \text{(Eq 6)}$$

$$\frac{\sigma}{A_1 + B_1\varepsilon + B_2\varepsilon^2} = (1 + C_1 ln\dot{\varepsilon}^*) \quad \text{(Eq 7)}$$

The coefficient of C_1 is found by the slope of the graph ($\sigma/A_1 + B_1\varepsilon + B_2\varepsilon^2$— $ln\dot{\varepsilon}^*$) given in Fig. 15b. The coefficient of C was found to be − 0.2697 according to the average of the slopes determined according to the different strain values.

Equation 8 is created in order to determine the λ_1 and λ_2 coefficients of the m-JC material model.

$$\frac{\sigma}{(A_1 + B_1\varepsilon + B_2\varepsilon^2) * (1 + C_1 ln\dot{\varepsilon}^*)} = \exp[\lambda(T - T_r)] \quad \text{(Eq 8)}$$

Equation 9 is obtained by taking the natural logarithm of both sides of Eq. 8.

$$ln\left[\frac{\sigma}{(A_1 + B_1\varepsilon + B_2\varepsilon^2) * (1 + C_1 ln\dot{\varepsilon}^*)}\right] = \lambda(T - T_r) \quad \text{(Eq 9)}$$

The λ values are found by determining the slopes of the graph at four different strain rate values ($ln\left[\frac{\sigma}{(A_1+B_1\varepsilon+B_2\varepsilon^2)*(1+C_1 ln\dot{\varepsilon}^*)}\right]$- $(T - T_r)$). λ_1 and λ_2 are found from the relationship between λ values determined for different strain rates and deformation temperatures and $ln\dot{\varepsilon}^*$. The intersection value gave λ_1 and the slope value gave λ_2. The graph of λ— $ln\dot{\varepsilon}^*$ is given in Fig. 15c and λ_1 =– 0.0041, λ_2 = − 0.0002.

The equation obtained with the Modified Johnson–Cook material parameters created is given below (Eq. 10).

$$\sigma = \left(145,09 + 2260 - 6982,9\varepsilon^2\right)(1 - 0,269 ln\dot{\varepsilon}^*) \exp[(-0,004 - 0,0002 ln\dot{\varepsilon}^*)(\mathrm{T} - \mathrm{Tr})] \quad \text{(Eq 10)}$$

3.5 Evaluation of Material Models

Correlation coefficients (R) and mean error levels (E) were calculated in order to determine the accuracy of the models obtained:

$$E(\%) = \left|\frac{\sigma_{predict} - \sigma_{exp}}{\sigma_{exp}}\right| x100 \quad \text{(Eq 11)}$$

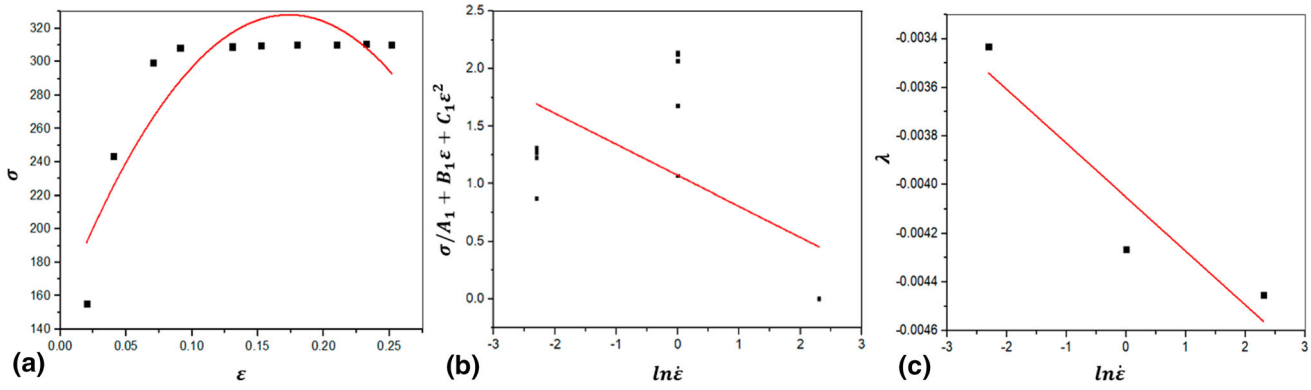


Fig. 15 (a) σ-ε graph, (b) [(σ/ $A_1 + B_1\varepsilon + B_2\varepsilon^2$) – ($ln\dot{\varepsilon}^*$)] relationship at 750 °C, c)λ - $ln\dot{\varepsilon}^*$ graph

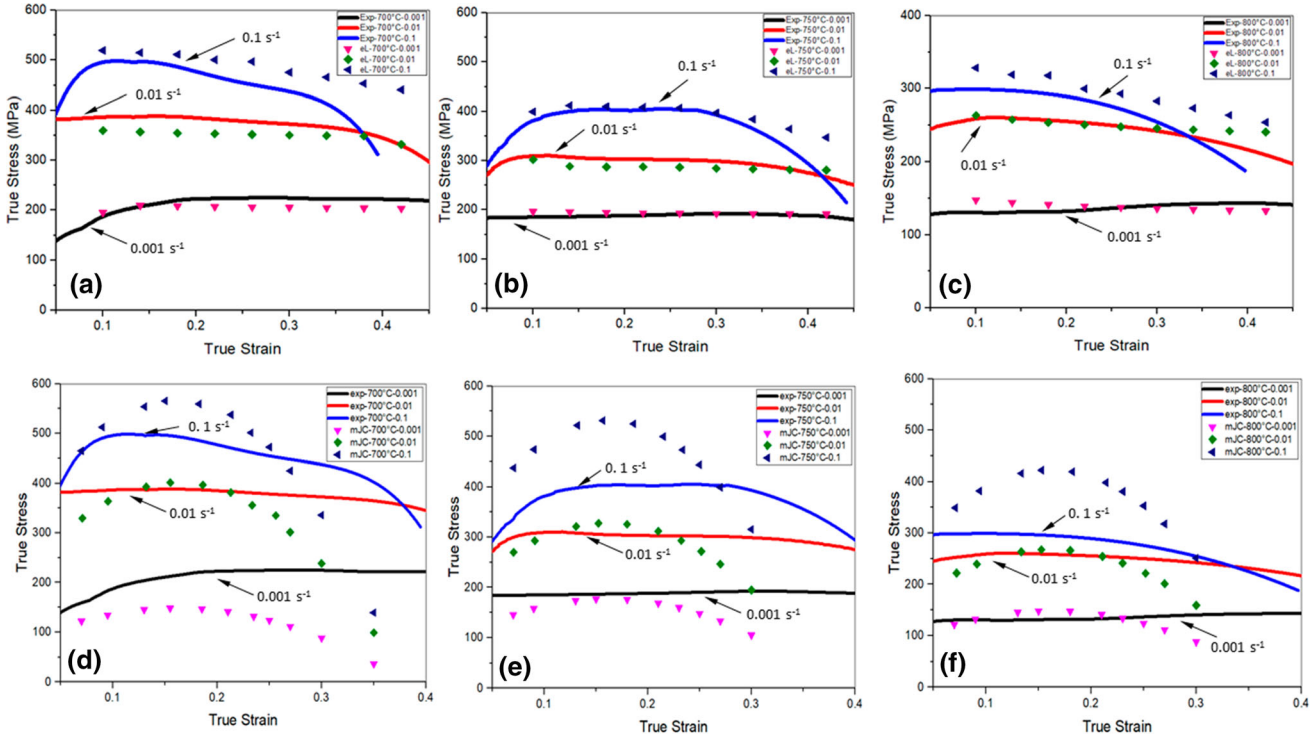


Fig. 16 (a) at 700 °C, (b) at 750 °C, (c) at 800 °C, comparing the calculated and experimental stress values according to e-Ludwik model, (d) at 700 °C, (e) at 750 °C, (f) at 800 °C, comparing the calculated and experimental stress values according to m-Johnson Cook model

$$R = \frac{\sum_{i=1}^{i=N}\left(\sigma_{exp}^{i} - \overline{\sigma}_{exp}\right)\left(\sigma_{p}^{i} - \overline{\sigma}_{p}\right)}{\sqrt{\sum_{i=1}^{i=N}\left(\sigma_{exp}^{i} - \overline{\sigma}_{exp}\right)^{2}\sum_{i=1}^{i=N}\left(\sigma_{p}^{i} - \overline{\sigma}_{p}\right)^{2}}} \quad \text{(Eq 12)}$$

Figure 16a-c shows the comparison of the stress data calculated according to the Extended Ludwik model with the experimental stress data, while Fig. 16d-f also shows the comparison of the experimental stress values with the stress values calculated according to the modified Johnson Cook material model. As can be clearly seen from the figures, the predictions of the Extended Ludwik model are higher. As can be seen from the comparison, the accuracy of the stress values estimated according to the mJC model is low, especially at the strain rate of 0.1 s^{-1}.

The correlation coefficient (R) was calculated to determine the accuracy of the structural equation. As it can be seen in Fig. 17a, the correlation coefficient of extended Ludwik was found to R = 0.988 which indicated that the model is built with high accuracy. The same procedure was applied to mJC and the correlation coefficient was found to be 0.89 (Fig. 17c).

Another procedure to examine the compatibility of the models with the experimental results was to determine the mean error levels. The mean error levels of Extended Ludwik stress values in Fig. 17b and Modified Johnson–Cook values in Fig. 17d are given as percentages. Mean error levels are higher at 0.1 s^{-1} strain rate for both models. For Extended Ludwik, mean error level is below 5% at all strain rate values, especially at 750 °C. In general, Extended Ludwik mean error rates are acceptable, but only exceeded 10% at 0.1 s^{-1} strain rate. When the mean error levels of the modified Johnson–Cook model are examined, it can be seen that it is high at 0.1 strain rate. Mean error levels are higher than Extended Ludwik, although at 0.001 and 0.01 strain rates, 10% at 750 and 800 °C. The main reason for the high error rate of the modified Johnson–Cook model may be that it is generally used to model flow behaviors with a peak. Therefore, it could not accurately predict the thermal softening effect. However, in the Extended Ludwik model, the thermal softening effect could be expressed more accurately. In the Extended Ludwik model, the strain rate precision is obtained from the coefficients in the equation. It is seen that the desired steady state flow behavior, especially for hot forming, is predicted much more reliably in this model. The main reason for the higher temperature sensitivity is because different values are included in the solution for each temperature. As a result, a model with both temperature and deformation rate sensitivity is presented. From the results obtained, it is suggested to use the Extended Ludwik model of Ti-6Al-4V in the range of 700-800 °C to predict the flow behavior.

This work provides guidance for the hot forming of titanium and its alloys with contribution to the literature from a comparative perspective in phenomenological modeling. However, it would be definitely insightful to support the findings with a case study from an industrial application, which is a topic of an upcoming study in progress.

4. Conclusions

In this study, uniaxial tensile tests at strain rates of 0.1, 0.01 and 0.001 s^{-1} at a range of 500 °C to 800 °C were applied to investigate the high-temperature forming of the Ti-6Al-4V

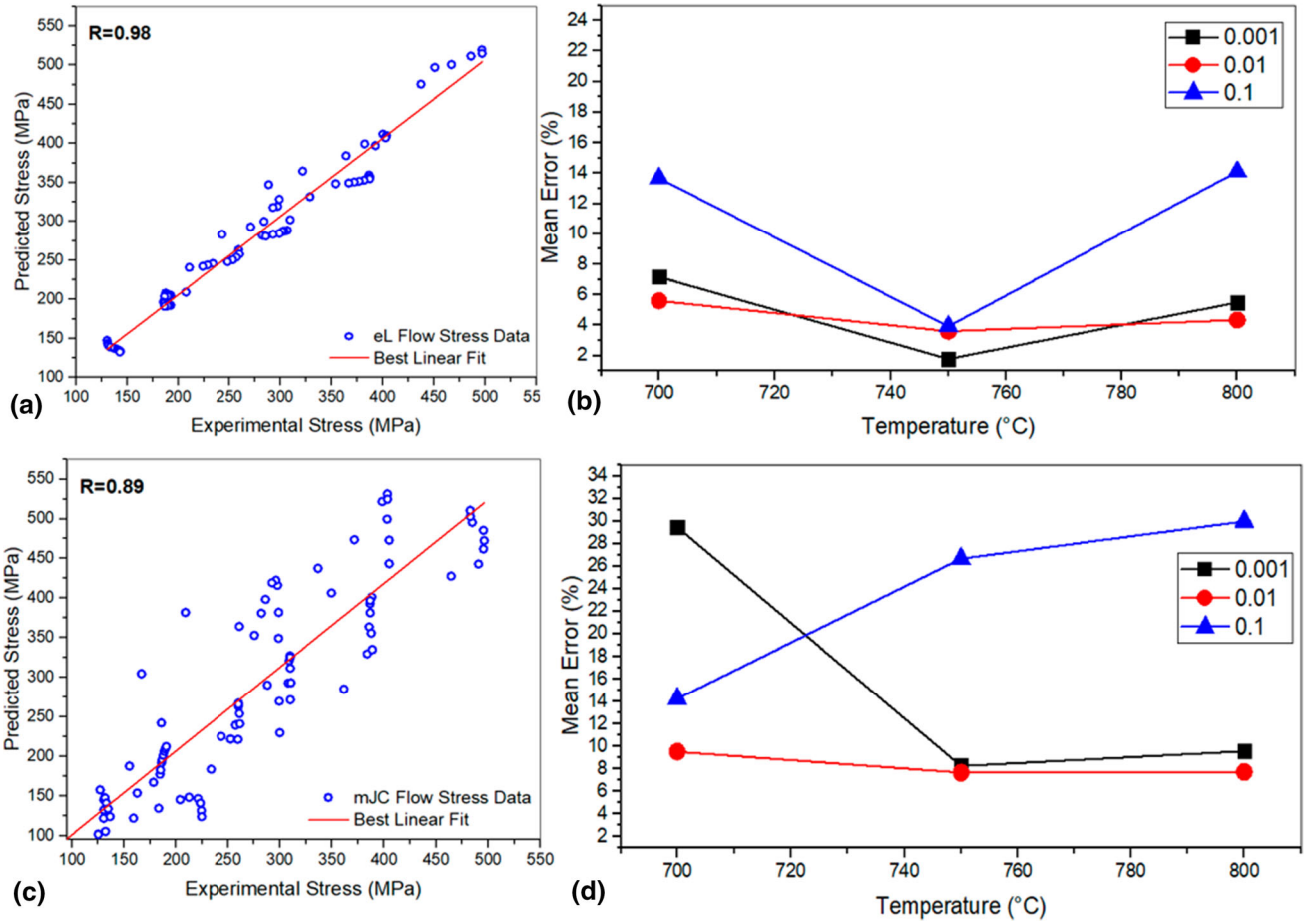


Fig. 17 Comparison between experimental and predicted data by two models: (a) e-Ludwik and (c) m-JC, mean error levels of (b) e-Ludwik and (d) m-JC

alloy. Thermomechanical behavior is modeled by two different empirical approaches where the following conclusions can be drawn:

1) With increasing temperature, the strength of the Ti-6Al-4V alloy decreased and the elongation at break increased. It has been reported that the yield strength is slightly above 100 MPa and the elongation at break is 0.85, especially under the test conditions of 0.001 s^{-1} at 800 °C. These values are ideal for the hot forming process.
2) According to the fracture surfaces analysis, it was determined that the fracture surface area decreased with increasing temperature, and similarly, decreasing the strain rate also decreased the fracture surface area.
3) The microstructural examination revealed that the β volume ratio and α grain size increased as the β transus temperature is approached.
4) The correlation coefficient (R) of the developed extended-Ludwik equation was calculated as 0.9858. The model, which gives a very high accuracy, especially at strain rates of 0.001 and 0.01 s^{-1} and at 750 and 800 °C, can be used as an empirical model for hot forming of Ti-6Al-4V.

Acknowledgements

This study was supported by the Scientific and Technological Research Council of Turkey (Turkish Aerospace Industries-Yıldız Technical University 2244—Industrial PhD Fellowship Program/ project number: 118C071) and the Scientific Research Program of Turkish Aerospace Industries. Partial support of the Ozyegin University Research Fund is also acknowledged.

Conflict of interest

The authors declare that they have no conflict of interest.

References

1. E.O. Ezugwu, J. Bonney and Y. Yamane, An Overview of the Machinability of Aeroengine Alloys, *J. Mater. Process. Technol.*, 2003, **134**(2), p 233–253. https://doi.org/10.1016/S0924-0136(02)01042-7
2. Hadavi, M. (2009): Advanced Materials in Aircraft İndustry. Materials. *Malek Ashtar Univ. Technol*
3. M.H. Yoo, J.R. Morris, K.M. Ho and S.R. Agnew, Nonbasal Deformation Modes of HCP Metals and Alloys: Role of Dislocation Source and Mobility, *Metall. Mater. Trans. A Phys. Metall. Mater. Sci.*, 2002, **33**(3), p 813–822. https://doi.org/10.1007/s11661-002-0150-1
4. M. Vanderhasten, L. Rabet and B. Verlinden, Ti-6Al-4V: Deformation Map and Modelisation of Tensile Behaviour, *Mater. Des.*, 2008, **29**(6), p 1090–1098. https://doi.org/10.1016/j.matdes.2007.06.005

5. P.E. Markovsky, J. Janiszewski, V.I. Bondarchuk, O.O. Stasyuk, D.G. Savvakin, M.A. Skoryk and S.V. Prikhodko, Effect of Strain Rate on Microstructure Evolution and Mechanical Behavior of Titanium-based Materials, *Metals*, 2020, **10**(11), p 1404.
6. G. Chen, C. Ren, X. Qin and J. Li, Temperature Dependent Work Hardening in Ti-6Al-4V Alloy Over Large Temperature and Strain Rate Ranges: Experiments and Constitutive Modeling, *Mater. Des.*, 2015, **83**, p 598–610. https://doi.org/10.1016/j.matdes.2015.06.048
7. B. Valoppi, S. Bruschi and A. Ghiotti, High-Temperature Mechanical Properties and Constitutive Modelling of Ti6Al4V Sheets, *Mater. Sci. Forum*, 2017, **879**, p 1980–1986. https://doi.org/10.4028/www.scientific.net/MSF.879.2020
8. S. Gao et al., Anisotropic Behavior and Mechanical Properties of Ti-6Al-4V Alloy in High Temperature Deformation, *J. Mater. Sci.*, 2022, **57**(1), p 651–670. https://doi.org/10.1007/s10853-021-06569-8
9. S. Dineshkumar, S. Sriram, R. Surendran and V. Dhinakaran, Experimental Investigation of Tensile Properties of Ti-6Al-4V Alloy at Elevated Temperature, *Int. J. Recent Technol. Eng.*, 2019, **8**(1), p 103–107.
10. R. Pederson, R. Gaddam and M.L. Antti, Microstructure and Mechanical Behavior of Cast Ti-6Al-4V with Addition of Boron, *Cent. Eur. J. Eng.*, 2012, **2**(3), p 347–357. https://doi.org/10.2478/s13531-012-0004-6
11. H. Zhan, G. Wang, D. Kent and M. Dargusch, Constitutive Modelling of the Flow Behaviour of a β Titanium Alloy at High Strain Rates and Elevated Temperatures Using the Johnson-Cook and Modified Zerilli-Armstrong Models, *Mater. Sci. Eng. A*, 2014, **612**, p 71–79. https://doi.org/10.1016/j.msea.2014.06.030
12. G. Kang, Y. Dong, Y. Liu and H. Jiang, Macroscopic and Microscopic Investigations on Uniaxial Ratchetting of two-phase Ti-6Al-4V Alloy, *Mater. Charact.*, 2014, **92**, p 26–35. https://doi.org/10.1016/j.matchar.2014.02.014
13. J. Cai, K. Wang, P. Zhai, F. Li and J. Yang, A Modified Johnson-Cook Constitutive Equation to Predict Hot Deformation Behavior of Ti-6Al-4V Alloy, *J. Mater. Eng. Perform.*, 2015, **24**(1), p 32–44. https://doi.org/10.1007/s11665-014-1243-x
14. Y.C. Lin and X.M. Chen, A Critical Review of Experimental Results and Constitutive Descriptions for Metals and Alloys in Hot Working, *Mater. Des.*, 2011, **32**(4), p 1733–1759. https://doi.org/10.1016/j.matdes.2010.11.048
15. J. Porntadawit, V. Uthaisangsuk and P. Choungthong, Modeling of Flow Behavior of Ti-6Al-4V Alloy at Elevated Temperatures, *Mater. Sci. Eng. A*, 2014, **599**, p 212–222. https://doi.org/10.1016/j.msea.2014.01.064
16. S. Seo, O. Min and H. Yang, Constitutive Equation for Ti-6Al-4V at High Temperatures Measured using the SHPB Technique, *Int. J. Impact Eng.*, 2005, **31**(6), p 735–754. https://doi.org/10.1016/j.ijimpeng.2004.04.010
17. W.M. Van Haaften, B. Magnin, W.H. Kool and L. Katgerman, Constitutive Behavior of as-cast AA1050, AA3104, and AA5182, *Metall. Mater. Trans. A Phys. Metall. Mater. Sci.*, 2002, **33**(7), p 1971–1980. https://doi.org/10.1007/s11661-002-0030-8
18. A. Soni and A. Alankar, Analyses of Constitutive Behavior of As-Cast Aluminum Alloys AA3104, AA5182, and AA6111 During Direct Chill Casting Using Physically Based Models, *J. Eng. Mater. Technol.*, 2019 https://doi.org/10.1115/1.4042869
19. W.M. Van Haaften, W.H. Kool and L. Katgerman, Effect of Strain Rate and Thermal History on the Constitutive Behaviour of Al-Mg alloy AA 5182, *Mater. Sci. Technol.*, 2004, **20**(10), p 1233–1236. https://doi.org/10.1179/026708304225022151
20. G. Wei et al., Constitutive Modeling of Mg-9Li-3Al-2Sr-2Y at Elevated Temperatures, *Mech. Mater.*, 2015, **89**, p 241–253. https://doi.org/10.1016/j.mechmat.2015.05.006
21. ASTM B348/B348M-21 Standard Specification for Titanium and Titanium Alloy Bars and Billets
22. ASTM E8/E8M-11 Standard Test Methods For Tension Testing Of Metallic Materials, 2011
23. G. Deng, X. Zhao, L. Su, P. Wei, L. Zhang, L. Zhan and N. Tsuji, Effect of High Pressure Torsion Process on the Microhardness, Microstructure and Tribological Property of Ti6Al4V Alloy, *J. Mater. Sci. Technol.*, 2021, **94**, p 183–195.
24. F. Ozturk, R.E. Ece, N. Polat, A. Koksal, Z. Evis and J.Y. Sheikh-Ahmad, Application of Electric Resistance Heating Method on Titanium Hot Forming at Industrial Scale, *Arab. J. Sci. Eng.*, 2016, **41**(11), p 4441–4448.
25. Mahdavi, R., Emadoddin, E., & Abbasi, S. M. (2022). Effect of Initial Microstructure and Strain Rate on the Hot Deformation Behavior of ATI425 Alloy in Two-Phase α/β Region. *J. Mater. Eng. Perform.*, 1–12
26. V. Anil Kumar, A. Sarkar, R.K. Gupta, M.J.N.V. Prasad and S.V.S.N. Murty, Microstructure Evolution During High-temperature Deformation of Ti-5Al-5V-2Mo-1Cr-1Fe Alloy Under Compression, *J. Mater. Eng. Perform.*, 2021, **30**(5), p 3258–3272.
27. Y. Zhou, J. Zhou, Q. Shu, S. Li, F. Gongye, S. Long and H. Deng, Deformation Mechanism and Constitutive Consideration for Ti-5Al-5Mo-5V-3Cr-1Zr Alloy Compressed at Elevated Temperatures, *J. Mater. Eng. Perform.*, 2020, **29**(8), p 5104–5113.
28. A.O. Mosleh, A.V. Mikhaylovskaya, A.D. Kotov, J.S. Kwame and S.A. Aksenov, Superplasticity of Ti-6Al-4V Titanium Alloy: Microstructure Evolution and Constitutive Modelling, *Materials (Basel)*, 2019, **12**(11), p 1756. https://doi.org/10.3390/ma12111756
29. J.I. Qazi, J. Rahim, O.N. Senkov, A. Genc and F.H. Froes, Phase Transformations in Ti-6Al-4V-xH Alloys, *Metall. Mater. Trans. A Phys. Metall. Mater. Sci.*, 2001, **32**(10), p 2453–2463. https://doi.org/10.1007/s11661-001-0035-8
30. J. Luo, M. Li and W. Yu, Microstructure Evolution During High Temperature Deformation of Ti-6Al-4V Alloy, *Rare. Met. Mater. Eng.*, 2010, **39**(8), p 1323–1328. https://doi.org/10.1016/s1875-5372(10)60114-2
31. T. Zhang, Y. Liu, D.G. Sanders, B. Liu, W. Zhang and C. Zhou, Development of Fine-Grain Size Titanium 6Al-4V Alloy Sheet Material for Low Temperature Superplastic Forming, *Mater. Sci. Eng. A*, 2014, **608**, p 265–272. https://doi.org/10.1016/j.msea.2014.04.098
32. S. Gao, Y. Sang, Q. Li, Y. Sun, Y. Wu and H. Wang, Constitutive Modeling and Microstructure Research on the Deformation Mechanism of Ti-6Al-4V Alloy Under Hot Forming Condition, *J. Alloys Compd.*, 2022, **892**, 162128. https://doi.org/10.1016/j.jallcom.2021.162128
33. M.A. Wahed, A.K. Gupta, V. Sharma, K. Mahesh, S.K. Singh and N. Kotkunde, Material Characterization, Constitutive Modelling, and Processing Map for Superplastic Deformation Region in Ti-6Al-4V Alloy, *Int. J. Adv. Manuf. Technol.*, 2019, **104**(9–12), p 3419–3438. https://doi.org/10.1007/s00170-019-03956-z
34. P. Hu, Y. Liu, Y. Zhu and L. Ying, Crystal Plasticity Extended Models based on Thermal Mechanism and Damage Functions: Application to Multiscale Modeling of Aluminum Alloy Tensile Behavior, *Int. J. Plast.*, 2016, **86**, p 1–25. https://doi.org/10.1016/j.ijplas.2016.07.001
35. H. Chen, L. Zhang, J. Bao, H. Guo, X. Tao and Y. Ouyang, The Effect of Grain Boundary Energy on the Amorphous Forming Composition Range of Zr–Fe–Al Ternary System, *J. Non. Cryst. Solids*, 2016, **432**, p 277–284. https://doi.org/10.1016/j.jnoncrysol.2015.10.020
36. A.J.W. Johnson, C.W. Bull, K.S. Kumar and C.L. Briant, The İnfluence of Microstructure and Strain Rate on the Compressive Deformation Behavior of Ti-6Al-4V, *Metall. Mater. Trans. A Phys. Metall. Mater. Sci.*, 2003, **34**(2), p 295–306. https://doi.org/10.1007/s11661-003-0331-6
37. Y. Han, S. Yan, B. Yin, H. Li and X. Ran, Effects of Temperature and Strain Rate on the Dynamic Recrystallization of a Medium-High-Carbon High-Silicon Bainitic Steel During Hot Deformation, *Vacuum*, 2018, **148**, p 78–87. https://doi.org/10.1016/j.vacuum.2017.11.007
38. Giuliano, G., (2011): Superplastic Forming of Advanced Metallic Materials, Methods and Applications. Woodhead Publishing Series in Metals and Surface Engineering
39. Y.C. Lin et al., Effects of İnitial Microstructures on Hot Tensile Deformation Behaviors and Fracture Characteristics of Ti-6Al-4V Alloy, *Mater. Sci. Eng. A*, 2018, **711**, p 293–302. https://doi.org/10.1016/j.msea.2017.11.044
40. Plastic Deformation and Ductile Fracture of Ti-6Al-4V under Various Loading Conditions. Ohio State University, 2012
41. U. Bathini, T.S. Srivatsan, A. Patnaik and T. Quick, A Study of the Tensile Deformation and Fracture Behavior of Commercially Pure Titanium and Titanium Alloy: Influence of Orientation and Microstructure, *J. Mater. Eng. Perform.*, 2010, **19**(8), p 1172–1182. https://doi.org/10.1007/s11665-010-9613-5
42. F.Q. Li, J.H. Mo, J.J. Li, L. Huang and H.Y. Zhou, Formability of Ti-6Al-4V Titanium Alloy Sheet in Magnetic Pulse Bulging, *Mater. Des.*, 2013, **52**, p 337–344. https://doi.org/10.1016/j.matdes.2013.05.064

43. A. Orozco-Caballero, F. Li, D. Esque-De Los Ojos, M.D. Atkinson and J.Q. da Fonseca, On the Ductility of Alpha Titanium: The Effect of Temperature and Deformation Mode, *Acta Mater*, 2018, **149**, p 1–10. https://doi.org/10.1016/j.actamat.2018.02.022
44. S.V. Sajadifar and G.G. Yapici, Workability Characteristics and Mechanical Behavior Modeling of Severely Deformed Pure Titanium at High Temperatures, *Mater. Des.*, 2014, **53**, p 749–757.
45. E. Alabort, D. Putman and R.C. Reed, Superplasticity in Ti-6Al-4V: Characterisation, Modelling and Applications, *Acta Mater.*, 2015, **95**, p 428–442. https://doi.org/10.1016/j.actamat.2015.04.056
46. Ludwik, P. (1909): Elemente der Technologischen Mechanik. *Jul. Springer, Berlin*
47. van Haaften, L. K. W.M., Magnin, B., Kool, W.H. (1999): Thermo-mechanical Behaviour of an AA3004 Alloy at Low Strain Rate. *Light Met.*
48. Fracture Characteristics of Three Metals Subjected to Various Strains, Strain Rates, Temperatures and Pressures. *G. R. Johnson W. H. Cook*, vol. Eng. Fract, 1985
49. H.Y. Li, Y.H. Li, X.F. Wang, J.J. Liu and Y. Wu, A comparative Study on modified Johnson Cook, modified Zerilli-Armstrong and Arrhenius-type Constitutive Models to Predict the Hot Deformation Behavior in 28CrMnMoV Steel, *Mater. Des.*, 2013, **49**, p 493–501. https://doi.org/10.1016/j.matdes.2012.12.083

Publisher's Note Springer Nature remains neutral with regard to jurisdictional claims in published maps and institutional affiliations.